Title: Heterogeneous photo-Fenton degradation of organics using highly efficient Cu-doped $LaFeO_3$ under visible light

Authors: Thi To Nga Phan, Aleksandar N. Nikoloski, Parisa Arabzadeh Bahri, Dan Li

PII: S1226-086X(17)30651-2
DOI: https://doi.org/10.1016/j.jiec.2017.11.046
Reference: JIEC 3756

To appear in:

Received date: 4-10-2017
Revised date: 24-11-2017
Accepted date: 29-11-2017

Please cite this article as: Thi To Nga Phan, Aleksandar N.Nikoloski, Parisa Arabzadeh Bahri, Dan Li, Heterogeneous photo-Fenton degradation of organics using highly efficient Cu-doped LaFeO3 under visible light, Journal of Industrial and Engineering Chemistry https://doi.org/10.1016/j.jiec.2017.11.046

Heterogeneous photo-Fenton degradation of organics using highly efficient Cu-doped $LaFeO_3$ under visible light

Thi To Nga Phan, Aleksandar N. Nikoloski, Parisa Arabzadeh Bahri, Dan Li*

Chemical and Metallurgical Engineering and Chemistry, School of Engineering and Information Technology, Murdoch University, Western Australia

*Corresponding author. Telephone: +61 8 9360 2569; E-mail: l.li@murdoch.edu.au.

Graphical abstract

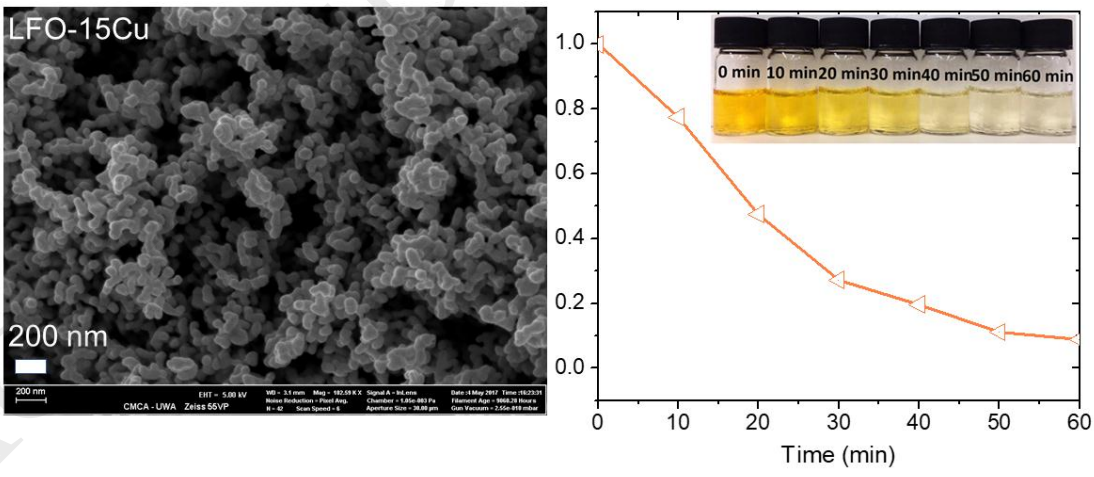

Highlights

- Cu-doped $LaFeO_3$ was studied as catalyst for Fenton-degradation of organics
- It was much more effective in degrading organic compared with undoped $LaFeO_3$
- The mechanism for photo-Fenton degradation was studied
- Its application was optimized in terms of solution pH, H_2O_2 and catalyst dosage
- The excellent stability and reusability suggested its potential for practical use

Abstract

Cu-doped $LaFeO_3$ was prepared by a facile hydrothermal reaction and evaluated as highly efficient photo-Fenton-like catalyst under visible light for organic degradation. The use of LFO-15Cu ($LaFe_{0.85}Cu_{0.15}O_3$), which possessed favourable physicochemical characteristics, could achieve almost complete decolourisation of cation and anion dyes within 60 min visible light irradiation. The mechanism study by ESR spectroscopy confirmed LFO-15Cu could activate H_2O_2 under visible light to generate many more hydroxyl radicals than LFO ($LaFeO_3$). LFO-15Cu was proven with excellent stability and reusability; and in turn showed great potential for use in continuous photo-Fenton-like degradation of organic in water under visible light.

Keywords: Photo-Fenton; Visible light; $LaFeO_3$; Copper; Methyl orange

1. Introduction

Organic dyes from textile production and other industrial processes are one of the main groups of pollutants in wastewater [1]. Azo dyes, including reactive black 5, methyl orange (MO), acid orange 7, represent 60 – 70% of all organic dyes produced in the world. The discharge of azo dye-containing effluent streams without treatment has created serious environmental pollution and threats to human health by releasing toxic and carcinogenic compounds [2]. Various methods, including biological, physical and chemical means, have been widely studied to eliminate azo dyes from wastewater [3]. In particular, advanced oxidation processes (AOPs) have become an increasing area of research interest for removing recalcitrant organic compounds in wastewater, due to its efficient and eco-friendly application. These processes rely on the production of strongly oxidising agents, mainly hydroxyl radicals (•OH), which are capable of oxidizing the majority of refractory compounds in industrial effluents due to the high oxidation potential (2.8 V) [4-7]. One of the most efficient AOPs is Fenton process, basically divided into the homogeneous and heterogeneous systems based on the physical state of catalyst. Compared to the homogeneous one, the heterogeneous Fenton process can oxidize a variety of organic pollutants in a wide pH range rapidly and non-selectively with the generation of little iron sludge. Other advantages include the complete mineralization of organic compounds and easy operation at mild condition [8-10]. The heterogeneous Fenton process involves the reaction between Fe-based solid catalyst and hydrogen peroxide (H_2O_2) to generate hydroxyl radicals (•OH), which are oxidants capable of degrading various organic contaminants in wastewater [11, 12]. In the presence of either ultraviolet (UV) irradiation, visible light or both these light sources, a photo-Fenton reaction occurs, which has higher degradation rate than the Fenton process [13]. As compared with the relatively high cost and energy consumption when utilizing light source to generate UV light, the adoption of visible light is more economical.

Recently, perovskite oxides with the general formula ABO_3 (A = usually an alkaline, alkaline earth or rare earth element; B = transition metal) have been recognized as an efficient form of heterogeneous catalysts to participate in the photo-Fenton process for the degradation of organic pollutants [14-17]. $LaFeO_3$ (LFO) is one of the widely selected perovskite oxides for study due to its non-toxicity, stability, and small band gap energy. Li and co-workers prepared the LFO heterogeneous photo-Fenton-like catalyst by sol-gel method for rhodamine B (RhB) degradation; in which over 97% of RhB was decomposed after 2 h visible light irradiation under the reaction conditions of 1 mL of 3% H_2O_2, 1 g/L catalyst and 10^{-5} mol/L initial RhB concentration [18]. The $LaMeO_3$ (Me = Fe, Co, Mn, Ni, Cu) perovskites supported on cordierite monolith, which were prepared by impregnation method, exhibited photo-Fenton activity to remove acetic acid; especially the use of 10.5 wt% LFO supported on cordierite monolith reached 93% TOC removal after 7 h under a variable addition of H_2O_2 (0.014 M/h after 1 h and 0.007 M/h in the rest of test) at pH = 3.9 under UV light irradiation [19]. Orak *et al.* prepared LFO on a monolithic structure by sol-gel method and yielded almost complete removal of methylparaben (MP) after 30 min under the reaction conditions of 0.1 g/L catalyst, 5 ppm MP, 1 mM of H_2O_2, initial pH 7 and UV light power of 12 W [20]. However, these photo-Fenton-like decontamination processes need a relatively long reaction time or special UV light source to complete. Therefore, we believe it is desirable to explore other heterogeneous photo-Fenton-like perovskite catalysts targeting at the fast and high removal of organic from water. Especially, from the point of view of practical application, the development of heterogeneous photo-Fenton process using visible light is particularly meaningful in terms of cost and energy effectiveness.

Replacing the element on the A- or B-site in the ABO_3 structure, which leads to the change in the composition and symmetry of material, is considered as a promising strategy to improve photocatalytic performance of a catalyst [21-23]. Such doping approach could not only

introduce defect to narrow band gap, but also cause oxygen vacancy inhibiting the recombination between photogenerated electrons and holes on the photocatalyst surface. Different metal ions through A- or B-site substitution of LFO have been proven to effectively improve its photo-Fenton catalytic activity for organic degradation [24-26]. Li and co-workers investigated the photocatalytic activity of Ca-doped $LaFeO_3$, which was prepared in reverse microemulsion, for the degradation of methylene blue (MB) under visible light [24]. The LFO sample doped with 10 mol% Ca exhibited the highest degradation rate (77.5%) in 60 min under the reaction conditions of 0.5 g/L catalyst dosage and 10 mg/L initial MB concentration among different Ca-doped LFO (5 – 20 mol%). The substitution of Li into La-site in LFO was found to considerably improve the photocatalytic performance of catalyst for the degradation of methyl blue and acrylon effluents [26]. The optimized catalyst, which was synthesized by the acetic acid based sol-gel method, could remove 99% methyl blue and 45.7% acrylon effluents in 60 min under UV-visible light illumination. Jauha *et al.* used Mn-doped LFO as a photo-Fenton catalyst to degrade anionic and cationic dyes, including Remazol Turquoise Blue, Remazol Brilliant Yellow, MB and Safranine-O, respectively [25]. Their results suggested that the photocatalytic activity under visible light irradiation be enhanced; however, the further increase of Mn doping did not considerably improve the photoactivity of resulting material.

Previous study has suggested that the catalytic property of ABO_3 be mainly determined by the nature of B-site [21]. Therefore, the substitution of Fe-site in LFO by a reductive and active metal shows potential to dramatically improve photocatalytic activity of resulting material. In our literature survey [27-30], in addition to Fe, other multiple redox state elements such as, cerium (Ce), manganese (Mg), chromium (Cr), copper (Cu) and cobalt (Co) can react with H_2O_2 to generate $^{\bullet}OH$ in the Fenton-like process. Especially, Cu attracted our research interest as a substituting cation due to its advantageous features over Fe [31-36]. For example, Cu endows high reducibility; the reduction of Cu(II) by H_2O_2 occurs more easily than that of

Fe(III). The Cu(I)/H_2O_2 system shows a higher reaction rate than the Fe(II)/H_2O_2 system in terms of organic decomposition. Moreover, a Cu-based Fenton-like system can work over a wider pH range than a Fe-based one. The use of Cu as a dopant and its incorporation into the perovskite lattice has been proven to narrow the band gap and enhance the catalytic activity of parent perovskite, e.g. $LaCoO_3$, $LaAlO_3$ or $CaTiO_3$ [37-39]. To the best of our knowledge, no study has been reported on the applicability of Cu-doped LFO as a heterogeneous photo-Fenton catalyst for organic dye degradation under visible light. In this study, Cu-doped LFO was prepared by a facile one-step hydrothermal method, which shows advantageous features towards industrial application, e.g. low temperature, cost effectiveness and process simplicity. Its photo-Fenton-like catalytic activity for the decolorization of 10 mg/L MO, MB and RhB solution, which concentration has been normally adopted in the photodegradation test of different dyes over a variety of heterogeneous catalysts [40-46], under visible light was evaluated for the first time. Based on our experimental results, including the catalyst morphological, structural and chemical properties, and electron spin resonance (ESR) analysis, possible catalytic mechanisms of Cu-doped LFO that improved degradation efficiency were also developed. Its stability and reusability in the photo-Fenton catalytic degradation of MO was assessed, followed by the examination and optimization on the effects of H_2O_2 concentration, catalyst dosage and initial solution pH on material photocatalytic activity.

2. Experimental

2.1 Catalyst Preparation

Analytical grade $La(NO_3)_3.6H_2O$, $Fe(NO_3)_3.9H_2O$, $Cu(NO_3)_2.3H_2O$ and citric acid were purchased from Sigma-Aldrich and used as the starting materials. Cu-doped $LaFeO_3$ ($LaFe_{1-x}Cu_xO_3$; x = 5, 10, 15 and 20 mol% of Cu) was prepared *via* the hydrothermal method [47]. Typically, the precursor solution was prepared by mixing $La(NO_3)_3.6H_2O$, $Cu(NO_3)_2.3H_2O$,

$Fe(NO_3)_3.9H_2O$, and citric acid in deionized (DI) water. Both the molar concentration of citric acid and the total molar concentration of metal nitrates ($La(NO_3)_3.6H_2O$, $Cu(NO_3)_2.3H_2O$, $Fe(NO_3)_3.9H_2O$) were 1 mol/L, respectively. The obtained precursor solution was continuously stirred for 2 h at room temperature. Ammonia solution (25%, Sigma-Aldrich) was slowly added to the solution to adjust the solution pH to 9 before transferring the resulting solution into 50 mL Teflon-lined autoclave. The solution was then heated at 180 °C for 20 h. After that, the autoclave was allowed to cool down to 25 °C naturally. The obtained product was washed with DI water and ethanol, and dried at 80 °C for 5 h in air. It was then calcined in air at 800 °C for 6 h (ramp rate of 5 °C/min from 25 to 800 °C) to obtain the final catalyst. The prepared catalysts were named as LFO-5Cu, LFO-10Cu, LFO-15Cu and LFO-20Cu, respectively, according to 5, 10, 15 and 20 mol% Cu doping concentration in the synthetic solution. For comparison, the $LaFeO_3$ catalyst (LFO-0Cu) was synthesized following the above procedures but without adding $Cu(NO_3)_2.3H_2O$ during synthesis.

2.2 Catalyst Characterization

Morphology of the catalysts was examined by scanning electron microscopy (SEM, 5 kV, Zeiss 1555, VP-FESEM) and transmission electron microscopy (TEM, 200 kV, TEM-TITAN). The powder sample was coated by sputtering of a thin platinum layer before performing SEM. The sample for TEM was dispersed in ethanol and then deposited on a carbon-copper grid to allow the solvent to evaporate at ambient temperature. X-ray powder diffraction (XRD) experiments were performed on a GBC eMMA X-ray diffractometer with Cu Kα radiation using an acceleration voltage of 35 kV and a current of 28 mA. The diffraction angle 2θ was scanned from 20 to 80 ° at a rate of 1 °/min. Average crystallite size of the sample was calculated from the XRD patterns according to the Scherrer equation [48, 49]. Lattice parameters of the sample were determined using the Bragg's law and the equation $\frac{1}{d^2} = \frac{h^2}{a^2} + \frac{k^2}{b^2} + \frac{l^2}{c^2}$ [50] (d is lattice spacing (Å); h, k, l are lattice planes and a, b, c are lattice parameters (Å)). The cell volume

was obtained by $a \times b \times c$ due to its orthorhombic structure. Nitrogen adsorption-desorption isotherms were measured at 77 K using SAPA2010 (Micromeritics Inc, USA). Prior to analysis, the samples were degassed at 200 °C for 12 h under vacuum. The surface area was determined from the linear part of the BET plot (P/P_0 = 0.05 ~ 0.20) and the pore size was calculated from the desorption branch of the isotherm by using Barrett-Joyner-Hallenda (BJH). The total pore volume was evaluated from the adsorbed nitrogen amount at a relative pressure of 0.98. Compositions of the catalysts were determined by chemical analysis using Inductively Coupled Plasma – Mass Spectrometry (ICP-MS, PerkinElmer's NexION 350). The digestion of sample was conducted by mixing 0.005 g of catalyst with 10 mL of aqua regia, followed by heating at 100 °C for 24 h. The digested sample was diluted with 2% HNO_3 to lower its concentration below 100 ppb for ICP-MS analysis. X-ray photoelectron spectroscopy (XPS) data were taken on Kratos AXIS Ultra DLD X-ray photoelectron spectroscopy (Perkin-Elmer) using a monochromated Al-Kα X-ray source ($h\upsilon$ = 1486.6 eV) at chamber pressured better than 8 x 10^{-9} Torr. Optical properties of the samples were characterized on a Perkin Elmer Lambda 750 UV/Vis/NIR spectrophotometer mounted with an integrating sphere accessor and using $BaSO_4$ as a reference. Band gap energy of the sample was obtained from the plot of Kubelka-Munck function $[F(R)h\upsilon]^2$ *versus* the energy of adsorbed light $h\upsilon$ [51].

2.3 Photocatalytic Organic Degradation and its Mechanism Study

Photocatalytic activity of the catalyst leading to the degradation of methyl orange (MO) (details in Fig. S1) in aqueous solution was carried out under visible light. The degradation experiment was performed in a cylindrical Pyrex vessel surrounded by a circulating water jacket to keep the reaction temperature at ambient temperature. The catalyst was dispersed into 100 mL of 10 mg/L MO aqueous solution. A photo-Fenton reaction was initiated by introducing 1 mL H_2O_2 to the suspension. A Xenon lamp (CEL-HX F300, Beijing, China) with a 400 nm cut-off filter to ensure the suspension was illuminated under visible light for photocatalytic degradation test.

In all photodegradation tests, the illuminated area of solution was 24 cm^2 and the intensity of light was 1734 W/m^2, which was measured by TES 132-Solar power meter (US). Before light irradiation, the solution was magnetically stirred in the dark for 30 min to reach the adsorption-desorption equilibrium of MO onto the catalyst. Subsequently, the suspension was exposed to visible light for 60 min, during which the sample was taken from the suspension every 10 min for analysis. The catalyst was removed from each analysis sample by centrifugation at 10,000 rpm for 10 min. The remaining solution was tested for the concentration of MO using Perkin Elmer Lambda 750 UV/Vis spectrometer and examined for the concentration of metal ions (La, Fe, and Cu) using ICP-MS (PerkinElmer's NexION 350). Several factors, including the catalyst dosage, the initial H_2O_2 concentration, the initial solution pH and co-existing inorganic salt NaCl were studied herein. The catalyst dosage was varied from 0.5 to 1.2 g/L. The initial solution pH value was adjusted from 4 to 8 by adding HCl or NaOH solution. The effect of H_2O_2 dosage on the degradation of MO was examined by varying the initial concentration from 0.1 to 0.5 g/L. To investigate the effect of co-existing ion on the photodegradation of MO, 0.01 M NaCl was added into the solution.

The photodegradation data were fitted with the pseudo-first-order kinetic model. The apparent rate constant k was obtained from the slope of the straight line by plotting $-\ln(C/C_0)$ as a function of time, t, through regression; where C_0 and C were the initial dye concentration and the dye concentration at a given period of time t, respectively. Herein, the corresponding regression coefficients R^2 were above 0.975. In addition to MO, MB and RhB (details in Fig. S1) were chosen to further evaluate the photo-Fenton catalytic performance of LFO-15Cu following the same procedures as above.

To test stability and recyclability of the catalyst, repetitive degradation test was performed using LFO-15Cu. After the degradation experiment, the suspension was centrifuged at 10,000

rpm to separate the catalyst particles and aqueous solution. The collected catalyst was then reused in a new degradation experiment. This process was repeated for several times.

Electron spin resonance (ESR) spectroscopy was used to examine photodegradation mechanism by detecting reactive oxygen species. Three conditions were selected herein for test, including LFO-15Cu/H_2O_2/Light (10 mg/L MO solution with 0.8 g/L LFO-15Cu in the presence of 0.3 g/L H_2O_2 under visible light irradiation), LFO-15Cu/H_2O_2/Dark (10 mg/L MO solution with 0.8 g/L LFO-15Cu in the presence of 0.3 g/L H_2O_2 in dark) and LFO/H_2O_2/Light (10 mg/L MO solution with 0.8 g/L LFO-0Cu in the presence of 0.3 g/L H_2O_2 under visible light irradiation). In 2 minutes after starting the reaction, 100 µL of the sample was collected from the reaction suspension and immediately mixed with 20 µL of 0.2 mol L^{-1} DMPO to form DMPO-˙OH adduct. The ESR spectra were obtained on a Bruker ESR 300E with microwave bridge (receiver gain: 40 dB; modulation amplitude: 1 Gauss; microwave power: 2.10^{-4} mW; modulation frequency: 100 kHz).

3. Results and Discussion

3.1 Catalyst Characterization

3.1.1 XRD analysis

As shown in Fig. 1, the crystal structures of $LaFe_{1-x}Cu_xO_3$ samples (LFO-5Cu – LFO-20Cu) were not affected by the presence of Cu dopants, as all peaks were identical to that of LFO (LFO-0Cu). The characteristic diffraction peaks at 22.6°, 32.2°, 38.0°, 39.6º, 46.3°, 52.0°, 53.3º, 57.4°, 67.4º, 72.0º and 76.7º in the diffraction data of all samples can be indexed as the crystal planes of (101), (121), (112), (220), (202), (141), (311), (240), (242), (143) and (204), indicating that the fabricated samples were well crystallized with orthorhombic structure (JCPDS No. 37-1493) [52, 53]. No crystalline Cu peaks were observed and the single

perovskite phase formed in all cases (LFO-5Cu – LFO-20Cu). However, the increase of Cu doping decreased the intensity of diffraction peaks and broadened them.

Table 1 shows the lattice parameters, cell volumes and average crystallite sizes of LFO and $LaFe_{1-x}Cu_xO_3$. As can be seen, the cell volume of $LaFe_{1-x}Cu_xO_3$ was slightly smaller than that of LFO; this value decreased with increasing Cu doping. Obviously, the introduction of Cu(II) with larger ionic radius (0.730 Å) to replace Fe(III) with smaller ionic radius (0.645 Å) did not lead to the expansion of LFO unit-cell [54]. The smaller cell volume of $LaFe_{1-x}Cu_xO_3$ might be caused by the defects in the form of anionic vacancies, which maintained the electroneutrality in $LaFe_{1-x}Cu_xO_3$ [55]. In Table 1, the crystallite sizes of Cu-doped LFO samples were smaller than that of undoped sample and decreased with increasing amount of Cu dopant. This is in good agreement with the literature [56], revealing Cu doping could cause lattice distortion and suppress growth of large crystallites in the samples. The high degree of crystallinity with few defects helps to minimize the recombination of electron-hole pairs, leading to enhanced efficiency of photodegradation [57].

3.1.2 Nitrogen adsorption-desorption analysis

In the N_2 adsorption-desorption isotherms of LFO and $LaFe_{1-x}Cu_xO_3$ samples (Fig. 2), all the samples showed type IV isotherms with type H3 hysteresis loop, where a steep increase was found in high-pressure range ($0.8 < P/P_0 < 1$). This could probably be associated with the pores formed between the particles due to aggregation. Table 2 summarizes the corresponding values of BET surface area, pore volume and pore size. The $LaFe_{1-x}Cu_xO_3$ samples, especially LFO-15Cu, exhibited slightly larger specific areas than the LFO sample; which might be the advantageous feature providing more active sites for the degradation to take place and improving photocatalytic degradation efficiency.

We believe that the addition of Cu source during hydrothermal synthesis would affect the crystallization of catalyst and in turn its structural properties. The possible mechanisms of $LaFe_{1-x}Cu_xO_3$ formation are proposed as follows based on the literature [58]:

$$La(NO_3)_3 \rightarrow La^{3+} + 3NO_3^- \quad (1)$$

$$Fe(NO_3)_3 \rightarrow Fe^{3+} + 3OH^- \rightarrow Fe(OH)_3 \quad (2)$$

$$Cu(NO_3)_2 \rightarrow Cu^{2+} + 2OH^- \rightarrow Cu(OH)_2 \quad (3)$$

$$La^{3+} + C_6O_7H_8 \rightarrow [C_6O_7H_5]^{3-}La^{3+} + 3H^+ \quad (4)$$

$$[C_6O_7H_5]^{3-}La^{3+} + 3OH^- \rightarrow La(OH)_3 + [C_6O_7H_5]^{3-} \quad (5)$$

$$La(OH)_3 + Fe(OH)_3 + Cu(OH)_2 \rightarrow LaFe_{1-x}Cu_xO_3 + H_2O \quad (6)$$

$La(NO_3)_3$ released La^{3+} when dissociated in water (Eq. 1), which tended to chelate with citric acid (Eq. 4). The resulting compound slowly reacted with hydroxide during hydrothermal reaction into $La(OH)_3$ *via* alcoholysis (Eq. 5). On the other side, $Fe(NO_3)_3$ and $Cu(NO_3)_2$ dissociated into Fe^{3+} and Cu^{2+}, which were then hydrolysed to produce $Fe(OH)_3$ and $Cu(OH)_2$ (Eq. 2 – 3). The condensation of $Cu(OH)_2$ – $Fe(OH)_3$ – $La(OH)_3$ system yielded Cu-doped LFO (Eq. 6). The increasing addition of Cu source in the synthetic solution might affect the condensation of $Cu(OH)_2$ – $Fe(OH)_3$ – $La(OH)_3$, and subsequent nucleation and crystallization of $LaFe_{1-x}Cu_xO_3$ during hydrothermal reaction. Consequently, small particles with large S_{BET} and small crystallite size were observed.

3.1.3 Band gap characterization

The UV-Vis absorption spectra and the corresponding band gap energy of LFO and $LaFe_{1-x}Cu_xO_3$ are shown in Fig. 3a and b. It is noted that all the samples had suitable band gap energy for organic pollutant degradation under visible light irradiation. Interestingly, the substitution of Cu into Fe-site in LFO modified the light absorption property of perovskite. Dong *et al.* also observed the decrease of gap energy when introducing Zn(II) (ionic radius = 0.74 Å) into LFO [59]. The substitution of metal in the Fe-site of LFO might lead to the formation of oxygen

vacancies and additional energy levels; thereby increasing the distance between atomics and narrowing the energy gap of material [59]. However, the high concentration of Cu doping (LFO-20Cu) resulted in an increase of band gap energy, accompanied with significantly reduced crystallite size (Table 1). The reduced band gap energy of $LaFe_{1-x}Cu_xO_3$ would be the favourable characteristic for harvesting more photons; more photocharged electrons and holes can be generated, thus enhancing the photocatalytic activity of catalysts.

3.1.4 Morphological analysis

As can be seen from Fig. 4, all the prepared samples exhibited similar morphology, consisting of agglomerated spherical-like particles. It is observed that the Cu-doping did not significantly affect the morphology and particle size of sample. However, when synthesized at high Cu doping concentration, the particles tended to merge together to form large agglomerates, as shown in Fig. 4. This may also explain the greater pore volumes and sizes, shown in Table 2, for the samples of LFO-15Cu and LFO-20Cu, when compared with others.

In the TEM images of LFO-0Cu and LFO-15Cu (Fig. 5), both samples showed sphere-like particles with diameters ranging from 30 – 70 nm, which is in an agreement with the SEM observation. Literature suggests small particle size as a favourable feature for enhancing photocatalytic activity because: (i) it results in large specific area, which may offer a large number of active sites for dye photodegradation; (ii) it helps to supress the recombination of photogenerated electron and hole pairs, which then migrate to particle surface and react with adsorbed dye [60]. There were no pure Cu particles observed on the surface of LFO-15Cu or in the surrounding environment, suggesting homogeneous substitution of Cu in the Fe-sites of LFO. The lattice fringes of LFO-0Cu and LFO-15Cu were 0.279 and 0.278 nm, respectively, which matched with the (121) crystallographic plane of LFO [53].

3.1.5 Composition analysis and XPS measurements

Table 2 shows the chemical compositions (Cu/Fe molar ratios) of LFO and $LaFe_{1-x}Cu_xO_3$ samples using ICP-MS analysis, suggesting that the actual Cu doping of $LaFe_{1-x}Cu_xO_3$ samples are consistent with the theoretical values.

To inspect the surface elemental composition and oxidation state of principal elements of LFO-15Cu as compared with LFO-0Cu, the typical XPS spectra of La 3d, Fe 2p, O 1s and Cu 2p are illustrated in Fig. 6. As can be seen, the spectrum in the La 3d region demonstrated a binding energy at 834.2 eV for La $3d_{5/2}$ and at 850.4 eV for La $3d_{3/2}$, implying that La had an oxidation state of +3 in LFO-15Cu and LFO-0Cu, which is in a good agreement with the literature [53, 56]. The La $3d_{5/2}$ peak revealed the typical complex structure of core-level photoemission spectra of light rare earth materials. The similarity for the peaks in the spectrum of La 3d region also suggests that the Cu doping did not significantly affect the chemical environment of La [56]. The O 1s spectrum presented two major peaks, suggesting that there be at least two kinds of O chemical states corresponding to the binding energy from 526.0 to 534.0 eV [56]. The binding energy of O 1s situated at 529.0 eV was due to the lattice oxygen species (O_L) in LFO-0Cu and LFO-15Cu. Meanwhile, the other broad peak (O_H) located at around 531.0 eV was mainly caused by a partial hydroxylation and/or carbonatation at the material surface [56, 61]. We note that there was a slight increase of intensity and broadening in the peak at 531.5 eV for the sample with Cu doping (LFO-15 Cu). It might be attributed to the enhanced hydroxylation and/or carbonatation onto the Cu-doped LFO material surface. The stable surface carbonates could block active sites and in turn suppressed photodegradation. On the other side, the higher surface hydroxylation was suggested increasing the number of active sites, thus favouring photodegradation [56]. The latter one is believed to play a dominating role herein when the reaction occurred in aqueous phase and seen from the following improved degradation results. Two strong peaks of Fe $2p_{3/2}$ and Fe $2p_{1/2}$ were located at 710.5 and 723.8 eV, respectively, which could be assigned to the +3 oxidation state of Fe in LFO-0Cu and LFO-15Cu [62]. There

was a slight shift of the Fe^{3+} peak in the LFO-15Cu spectrum, possibly caused by the change of Fe-O bond by introducing Cu in Fe-site [63]. In the Cu 2p spectrum of LFO-15Cu, the characteristic peaks of Cu $2p_{1/2}$ and Cu $2p_{3/2}$ located at 953.5 and 933.2 eV, respectively; and a satellite peak at 942.3 eV, which can be attributed to the +2 oxidation state of Cu [56, 64, 65]. The results of XPS spectra obviously indicate that the doping with Cu into LFO did not form other phases.

3.2. Photo-Fenton Degradation of MO

3.2.1. Copper doping on MO degradation

The photocatalytic activity of LFO and $LaFe_{1-x}Cu_xO_3$ was evaluated by the degradation of MO in the presence of visible light and H_2O_2. Before starting light illumination, the adsorption of MO onto LFO and $LaFe_{1-x}Cu_xO_3$ was found negligible, which was less than 3%. As can be seen in Fig. 7, the $LaFe_{1-x}Cu_xO_3$ samples exhibited much better catalytic activity for MO degradation than the LFO sample. As the amount of Cu doping increased, the MO degradation efficiency increased; but it suffered a decrease when using LFO-20Cu. There appear to be an optimum amount of Cu doping to obtain the maximum rate of photodegradation of MO, with the photocatalytic efficiency following the order: LFO-0Cu < LFO-5Cu < LFO-20Cu < LFO-10Cu < LFO-15Cu. The LFO-15Cu sample showed the highest catalytic activity with over 90% of MO removed after 60 min exposure to visible light, which is significantly greater than 33% of MO removed by LFO-0Cu. The pseudo-first-order model was used to better understand the reaction kinetic of MO degradation [40]. From the pseudo-first-order kinetic modelling (Fig. 7b), the apparent rate constant *k* was 0.0064, 0.0144, 0.0243, 0.0414, and 0.0195 /min for LFO-0Cu, LFO-5Cu, LFO-10Cu, LFO-15Cu and LFO-20Cu, respectively. The highest value of *k* was observed for LFO-15Cu, suggesting the fastest degradation rate and best photocatalytic activity.

Fig. 8 illustrates the time-dependent absorbance spectrum of LFO-15Cu in the MO photo-Fenton degradation; the inset shows the corresponding colour change of solution. As irradiation time increased, the absorption maximum of MO at λ = 464 nm steadily decreased. There was little change in the absorption maximum for LFO-15Cu after 50 min visible light irradiation. The MO photodegradation performance of LFO-15Cu was promising when compared with literature [45, 46, 66], although note that the reaction conditions varied. For example, LFO-15 Cu removed > 90% MO after 1 h visible light illumination under the conditions of temperature = 25 °C; initial dye concentration = 10 mg/L; catalyst dosage = 0.8 g/L; initial H_2O_2 concentration = 0.3 g/L; initial pH = 6. Under the similar conditions (temperature = 30 °C; initial dye concentration = 10 mg/L; dosage = 0.75 g/L; initial H_2O_2 concentration = 0.5 mol/L; initial pH = 6), the $H_3PW_{12}O_{40}$ supported Fe-bentonite (HPW-Fe-Bent) only degraded 78% MO after 1 h UV light irradiation [45].

Note that when no catalyst was added, the degradation of MO was only ~2% and 7% in the absence and presence of H_2O_2 after 60 min visible light irradiation (Fig. 7a). This suggests that MO itself was hardly degraded by H_2O_2 or light. In the other words, significant decolorization was observed under visible light illumination when both LFO-15Cu and H_2O_2 were present, which implies LFO-15Cu as a heterogeneous visible-light-excited Fenton-like catalyst. Taken account of excellent photo-Fenton catalytic performance, LFO-15Cu was chosen for all the following experiment.

3.2.2. Proposed mechanism for MO degradation

ESR spectroscopy was used to confirm the roles of •OH radicals in our experiments, with DMPO chosen as the scavenger of hydroxyl radicals which were generated during the photo-Fenton reaction. The same sample tube (size and type), DMPO concentration, and volume of DMPO adducts solution were used for all measurements; the intensity of EPR signals therefore depended only on the amount of •OH radicals. As can be seen from Fig. 9a, four characteristic

peaks of DMPO-OH adduct with the intensity of 1:2:2:1 were observed in LFO/H_2O_2/Light, LFO-15Cu/H_2O_2/Dark and LFO-15Cu/H_2O_2/Light, suggesting that hydroxyl radicals form in all three cases. The increase in signal intensity for LFO-15Cu/H_2O_2/Light as compared to that for LFO-15Cu/H_2O_2/Dark indicated that more $^{\bullet}OH$ radicals were generated when the system was illuminated by visible light than that in the dark condition. These results supported the suggestion that visible light irradiation enhanced the formation of hydroxyl radicals and thereby accelerated the photo-Fenton degradation of MO (as shown in Fig. 9b). For LFO/H_2O_2/Light, the peak intensity of DMPO-OH adducts appeared weaker than for LFO-15Cu/H_2O_2/Light when both were irradiated by visible light, indicating that LFO-15Cu enhanced the decomposition of H_2O_2 to generate a larger amount of $^{\bullet}OH$ radicals during the decolorization of MO. It was consistent with the observation in Fig. 9b, that the doping with Cu on LFO enhanced photocatalytic activity.

On the basis of above results and literature review, the MO degradation over LFO-15Cu likely occurred *via* two mechanisms as follows:

(a) The first pathway is suggested as a heterogeneous Fenton-like catalytic mechanism [67]. In a typical Fenton-like reaction, the commonly accepted mechanism is:

$$\equiv Fe^{III} + H_2O_2 \rightarrow \equiv Fe^{II} + HO_2^{\bullet} + H^+ \quad (7)$$

$$\equiv Fe^{III} + HO_2^{\bullet} + H^+ \rightarrow \equiv Fe^{II} + O_2 + 2H^+ \quad (8)$$

$$\equiv Fe^{II} + H_2O_2 \rightarrow \equiv Fe^{III} + {}^{\bullet}OH + OH^- \quad (9)$$

Similarly to Fe, Cu also activated H_2O_2 *via* the reactions as follows [33, 68]:

$$\equiv Cu^{II} + H_2O_2 \rightarrow \equiv Cu^{I} + H^+ + HO_2^{\bullet} \quad (10)$$

$$\equiv Cu^{II} + HO_2^{\bullet} + H^+ \rightarrow \equiv Cu^{I} + O_2 + 2H^+ \quad (11)$$

$\equiv Cu^{I} + H_2O_2 \rightarrow \equiv Cu^{II} + {}^{\bullet}OH + OH^{-}$ (12)

Photo-Fenton process is similar to the Fenton reaction, but also introduces light irradiation to improve the degradation. Under light illumination, the reduction of Fe(III) and Cu(II) can be accelerated, yielding additional reactive ${}^{\bullet}OH$ (Eq. (13, 14)), which can attack target organic [69].

$\equiv Fe^{III} + OH^{-} \rightarrow \equiv Fe^{III}(OH) + h\nu \rightarrow \equiv Fe^{II} + {}^{\bullet}OH$ (13)

$\equiv Cu^{II} + OH^{-} \rightarrow \equiv Cu^{II}(OH) + h\nu \rightarrow \equiv Cu^{I} + {}^{\bullet}OH$ (14)

The partial substitution of Cu(II) into Fe(III)-site in LFO-15Cu not only promoted the production of hydroxyl radicals but also led to the generation of more Fe(II) onto surface of the LFO-15Cu catalyst shown in Eq. (15) [68]:

$\equiv Fe^{III} + \equiv Cu^{I} \rightarrow \equiv Fe^{II} + \equiv Cu^{II}$ (15)

(b) The second pathway follows photocatalytic mechanism, in which LFO-15Cu absorbed the visible light and then underwent charge separation (Eq. (16)). Then the electrons were trapped by the H_2O_2 to generate ${}^{\bullet}OH$ (Eq. (17))

LFO-15Cu + $h\nu \rightarrow e_{cb}^{-} + h_{vb}^{+}$ (16)

$H_2O_2 + e_{cb}^{-} \rightarrow {}^{\bullet}OH + OH^{-}$ (17)

The electron-hole recombination (Eq. (18)) needs to be minimized for producing ${}^{\bullet}OH$.

$e_{cb}^{-} + h_{vb}^{+} \rightarrow energy$ (18)

Finally, the generated ${}^{\bullet}OH$ directly oxidized MO, as represented in Eq. (19):

$^{\bullet}OH + MO \rightarrow$ Degradation products (19)

As shown in Fig. 7, the highest value of *k* was observed for LFO-15Cu among a number of undoped and Cu-doped samples, suggesting the fastest degradation rate and best photocatalytic activity. This can be explained by its high specific surface area and low band gap energy, accompanied with good crystallinity and small particle size. These features benefit suppression of election-hole recombination and generation of $^{\bullet}OH$ radicals. Especially, a greater amount of $^{\bullet}OH$ radicals would form *via* the interaction of oxygen vacancies, which was caused by the substitution of Fe(III) by Cu(II), and water molecules adsorbed on the catalyst surface [56]. Furthermore, Cu and oxygen vacancies might act as electron traps reducing recombination of electron and hole; and in turn enhancing photodegradation.

3.3 Effects of Parameters on MO Degradation

3.3.1 Effect of catalyst dose on MO degradation

In Fig. 10, the photocatalytic efficiency of LFO-15Cu increased with increasing catalyst dosage up to 0.8 g/L and above that the degradation efficiency decreased. The observed apparent rate constant *k* for MO degradation at the catalyst dosage of 0.5, 0.8, 1.0, and 1.2 g/L was 0.0168, 0.0468, 0.04214, and 0.0217 /min, respectively. A possible explanation is that initially, the higher dosage of LFO-15Cu created more active sites and thus enhanced MO degradation. However, as the dosage increased further, an excessive amount of catalyst suppressed light penetration into the suspension, decreasing the photo-activation effect and in turn lowering the degradation rate.

3.2.3 Effect of initial pH on MO degradation

It is well-known that the initial pH value has a great influence on the photo-Fenton reaction because pH controls the generation of hydroxyl radicals. The effect of initial pH on MO degradation is illustrated in Fig. 11. The percentage of MO removal *via* the photo-Fenton

degradation decreased with increasing pH; this is consistent with the recent report [70]. A maximum degradation rate of 92.9% was achieved when using LFO-15Cu at pH = 6; whilst the degradation rate dropped to 85.9% at pH = 7 and 70.4% at pH = 8. The pseudo-first-order reaction rate constant *k* was found to be the highest (0.0468 /min) at pH = 6; as compared with 0.0313, 0.0338, 0.0346, and 0.0212 /min when at pH = 4, 5, 7, and 8, respectively. This could be explained by the form of MO existence which depends on the solution pH. In acidic solution, MO is in quinoid structure which is easier to be decomposed in comparison with that in azo structure formed at alkaline solution [71]. The increase of solution pH is also detrimental to the Fenton-like degradation process due to the decomposition of hydrogen peroxide into water and oxygen [72]. We found that the degradation rates of MO at pH 4 and 5 were both smaller than that at pH 6. This may be due to the fact that the catalyst's active sites are unstable in a more acidic media and copper just exhibits a dominant role in the Fenton reaction at pH > 4 [73]. On the other side, at the low pH, more H^+ ions were generated that could react with hydroxyl radicals $^{\bullet}OH$, leading to the decrease of degradation efficiency [73].

3.3.2 Effect of H_2O_2 concentration on MO degradation

The effect of H_2O_2 dosage on the degradation of MO was examined by varying the initial concentration from 0.1 to 0.5 g/L, with the results shown in Fig. 12. As the H_2O_2 concentration was increased from 0.1 to 0.3 g/L, the MO degradation rate also increased correspondingly from 78.8% to 92.9% with *k* increasing from 0.0260 to 0.0468 /min, because of increasing hydroxyl radicals in the solution. However, a decrease of MO degradation rate was observed when further increasing the concentration of H_2O_2 to 0.5 g/L. The pseudo-first-order reaction apparent rate constant *k* was found to attain an optimum value of 0.0468 /min in 0.3 g/L H_2O_2, and then decreased to 0.0412 /min when the H_2O_2 concentration rose up to 0.5 g/L. This is probably due to the fact that at a high H_2O_2 concentration, $^{\bullet}OH$ radicals can react with H_2O_2 to generate less reactive species such as hydroperoxyl radicals $HO_2^{\bullet}$ [46], following the reaction:

$$^{\bullet}OH + H_2O_2 \rightarrow HO_2^{\bullet} + H_2O$$

This reaction would compete with the dye degradation reaction, reduce the probability of MO attacked by $^{\bullet}OH$ radicals and subsequently lower dye removal rate.

3.3.3 Effect of co-existing ion on MO degradation

The effect of co-existing ion on the photo-Fenton degradation of MO is presented in Fig. 13. As is well known, inorganic ion such as chloride (Cl^-) is commonly present in the wastewater originated from dyestuff and textile industries; thus, its effect on photodegradation of MO cannot be neglected. Taking account of the negligible effect of Na^+ [74], our results revealed that Cl^- appeared to inhibit the MO removal by using LFO-15Cu. In the presence of 0.01 M Cl^-, only 62.8% MO (k = 0.0170 /min) was removed, which was much lower than that (92.9%; k = 0.0468 /min) when no Cl^- was added in the dye-containing solution. Cl^- might act as the scavenger of $^{\bullet}OH$ and h^+ [75], thus reducing the formation of hydroxyl radicals and lowering photodegradation efficiency. The presence of Cl^- in the solution exhibited a negative impact on the photodegradation of MO.

3.5 Stability and Reusability of Cu-doped LFO

The stability and reusability of LFO-15Cu was examined by reclaiming the catalyst after an initial MO degradation experiment, then using it as the catalyst with a fresh batch of MO, and repeating this for several times. The results are illustrated in Fig. 14.

LFO-15Cu demonstrated only a slight drop in removal efficiency of MO from 92.9% (1^{st} run) to 88.5% (4^{th} run), suggesting that it have good stability over repetitive photo-Fenton catalytic degradation of MO under visible light illumination. It was further supported by the XRD and ICP-MS analysis. After finishing 4 cycles of photo-Fenton catalytic degradation of MO, the structure of LFO-15Cu was almost unchanged based on the XRD patterns (Fig. 15). The ICP-

MS analysis showed only 1.558 mg/L La and 0.482 mg/L Cu in the solution after degradation test with little Fe observed, which suggests that metal leaching from the catalyst be negligible. Thus, LFO-15Cu was proven to be stable and reusable for MO degradation.

3.4 Evaluation of Cu-doped LFO on Degradation of Other Dyes

As can be seen above, excellent photo-Fenton catalytic degradation of MO was observed under the optimum conditions: 0.3 g/L H_2O_2 dosage and 0. 8 g/L catalyst loading at the initial solution pH 6. Under the same conditions, the photocatalytic performance of LFO-15Cu was also evaluated for the cationic dyes, RhB and MB.

Seen from Fig. 16, negligible removal of dye was induced by adsorption (3% for MO; 4.5% for MB; and 2% for RhB). Of these three dyes, MB showed the highest self-degradation and the oxidation by H_2O_2 under visible light, with the decolourization rate of 26% and 65%, respectively (Fig. 16). On the other side, a limited amount of RhB and MO (< 6%) was removed in the processes which were initiated solely by using visible light or H_2O_2. Our results showed that LFO-15Cu exhibited superior catalytic activity for the photodegradation of these dyes, with a removal rate of 99.4% for RhB, 98.8% for MB and 92.9% for MO (Fig. 16). The slightly lower photodegradation efficiency of MO might be attributed to its high chemical stability and low photosensitized property [76]. Similar observation was also reported in other studies [77, 78].

5. Conclusions

Cu-doped $LaFeO_3$ ($LaFe_{1-x}Cu_xO_3$) samples were prepared by a hydrothermal method and used as heterogeneous visible-light-driven Fenton-like catalysts for the degradation of methyl orange (MO). The results showed that LFO-15Cu with a theoretical 15 mol% Cu doping was more effective than the sample of $LaFeO_3$ (LFO) in terms of MO decolourisation. Under visible light irradiation, the use of 0.8 g/L LFO-15Cu induced 92.9% of MO removal in 60 min at the

initial H_2O_2 concentration of 0.3 g/L and initial pH of 6. The partial substitution of Cu into LFO improved MO degradation rate by approximately 60%; which could be ascribed to the formation of more •OH radicals during the decolorization of MO. The encouraging data also indicated the high stability and reusability of LFO-15Cu; therefore, it shows great potential as a promising catalyst for organic pollutant removal in the field of wastewater treatment.

Acknowledgement

T. Phan's PhD study is supported by Australia Awards Scholarship. This research was funded by Murdoch SEIT Small Grant Scheme (2016). The authors acknowledge the facilities, and the scientific and technical assistance of the Australian Microscopy & Microanalysis Research Facility at the Centre for Microscopy, Characterisation & Analysis, The University of Western Australia, a facility funded by the University, State and Commonwealth Governments. The authors thank Dr. Jakub Skut and Dr. Juita for EPR analysis; Ms Caitlin Sweeney and Dr Lihong Liu for band gap measurement and analysis.

References

[1] A. Touati, T. Hammedi, W. Najjar, Z. Ksibi, S. Sayadi, J. Ind. Eng. Chem., 35 (2016) 36-44.
[2] A. Bafana, S.S. Devi, T. Chakrabarti, Environ. Rev., 19 (2011) 350-371.
[3] T. Robinson, G. McMullan, R. Marchant, P. Nigam, Bioresour Technol., 77 (2001) 247-255.
[4] A. Aleboyeh, H. Aleboyeh, Y. Moussa, Dyes Pigm., 57 (2003) 67-75.
[5] S. Malato, J. Blanco, J. Cáceres, A.R. Fernández-Alba, A. Agüera, A. Rodríguez, Catal. Today, 76 (2002) 209-220.
[6] H. Zangeneh, A. Zinatizadeh, M. Habibi, M. Akia, M.H. Isa, J. Ind. Eng. Chem., 26 (2015) 1-36.
[7] N.M. Dang, K. Lee, J. Ind. Eng. Chem., In Press (2017).
[8] J.H. Ramirez, F.J. Maldonado-Hódar, A.F. Pérez-Cadenas, C. Moreno-Castilla, C.A. Costa, L.M. Madeira, Appl. Catal., B., 75 (2007) 312-323.
[9] A. Rodriguez, G. Ovejero, J. Sotelo, M. Mestanza, J. García, Ind. Eng. Chem. Res., 49 (2009) 498-505.
[10] S. Papić, D. Vujević, N. Koprivanac, D. Šinko, J. Hazard. Mater., 164 (2009) 1137-1145.
[11] O. Legrini, E. Oliveros, A. Braun, Chem. Rev., 93 (1993) 671-698.
[12] J. Xu, W. Wang, E. Gao, J. Ren, L. Wang, Catal. Commun., 12 (2011) 834-838.
[13] J.M. Chacón, M.T. Leal, M. Sánchez, E.R. Bandala, Dyes Pigm., 69 (2006) 144-150.
[14] T. Soltani, B.-K. Lee, J. Mol. Catal. A: Chem., 425 (2016) 199-207.
[15] T. Soltani, B.-K. Lee, Chem. Eng. J., 313 (2017) 1258-1268.
[16] B. Palas, G. Ersöz, S. Atalay, Process Saf. Environ. Prot., 111 (2017) 270-282.
[17] P. Granger, V.I. Parvulescu, V.I. Parvulescu, W. Prellier Eds., Wiley-VCH Verlag GmbH & Co. KGaA, (2016).
[18] L. Li, X. Wang, Y. Zhang, Mater. Res. Bull., 50 (2014) 18-22.
[19] D. Sannino, V. Vaiano, P. Ciambelli, L.A. Isupova, Catal. today, 161 (2011) 255-259.
[20] C. Orak, S. Atalay, G. Ersöz, Sep. Sci. Technol., 52 (2017) 1310-1320.
[21] M. Pena, J. Fierro, Chem. Rev. , 101 (2001) 1981-2018.
[22] F. Magalhães, F.C.C. Moura, J.D. Ardisson, R.M. Lago, Mater. Res., 11 (2008) 307-312.
[23] T. Soltani, B.-K. Lee, J. Hazard. Mater., 316 (2016) 122-133.
[24] F.-t. Li, Y. Liu, R.-h. Liu, Z.-m. Sun, D.-s. Zhao, C.-g. Kou, Mater. Lett., 64 (2010) 223-225.
[25] S. Jauhar, M. Dhiman, S. Bansal, S. Singhal, J. Sol-Gel Sci. Technol., 75 (2015) 124-133.
[26] L. Hou, G. Sun, K. Liu, Y. Li, F. Gao, J. Sol-Gel Sci. Technol., 40 (2006) 9-14.
[27] Y. Zhang, X. Dou, J. Liu, M. Yang, L. Zhang, Y. Kamagata, Catal. Today, 126 (2007) 387-393.
[28] A.D. Bokare, W. Choi, J. Hazard. Mater., 275 (2014) 121-135.
[29] X. Liang, Y. Zhong, H. He, P. Yuan, J. Zhu, S. Zhu, Z. Jiang, Chem. Eng. J. , 191 (2012) 177-184.
[30] Z. Han, Y. Dong, S. Dong, J. Hazard. Mater., 189 (2011) 241-248.
[31] L. Lyu, L. Zhang, C. Hu, Chem. Eng. J., 274 (2015) 298-306.
[32] C. Bao, H. Zhang, L. Zhou, Y. Shao, J. Ma, Q. Wu, RSC Adv., 5 (2015) 72423-72432.
[33] D.A. Nichela, A.M. Berkovic, M.R. Costante, M.P. Juliarena, F.S.G. Einschlag, Chem. Eng. J., 228 (2013) 1148-1157.
[34] F.L. Lam, A.C. Yip, X. Hu, Ind. Eng. Chem. Res., 46 (2007) 3328-3333.
[35] J.F. Perez-Benito, J. Inorg. Biochem., 98 (2004) 430-438.
[36] M.K. Eberhardt, G. Ramirez, E. Ayala, J. Org. Chem., 54 (1989) 5922-5926.
[37] H. Wang, L. Zhang, C. Hu, X. Wang, L. Lyu, G. Sheng, Chem. Eng. J., 332 (2018) 572-581.
[38] L. Wang, Q. Pang, Q. Song, X. Pan, L. Jia, Fuel, 140 (2015) 267-274.
[39] H. Zhang, G. Chen, Y. Li, Y. Teng, Int. J. Hydrogen Energy, 35 (2010) 2713-2716.
[40] Y. Hanifehpour, B. Soltani, A.R. Amani-Ghadim, B. Hedayati, B. Khomami, S.W. Joo, J. Ind. Eng. Chem., 34 (2016) 41-50.
[41] S. Park, J. Park, R. Selvaraj, Y. Kim, J. Ind. Eng. Chem., 31 (2015) 269-275.
[42] M.-T. Nguyen-Le, B.-K. Lee, D.-M. Tran, J. Ind. Eng. Chem., 56 (2017) 225-233.
[43] Y. Jiang, F. Li, Y. Liu, Y. Hong, P. Liu, L. Ni, J. Ind. Eng. Chem., 41 (2016) 130-140.
[44] S.A. Ansari, M.M. Khan, J. Lee, M.H. Cho, J. Ind. Eng. Chem., 20 (2014) 1602-1607.

[45] G.-T. Wei, C.-Y. Fan, L.-Y. Zhang, R.-C. Ye, T.-Y. Wei, Z.-F. Tong, Catal. Commun., 17 (2012) 184-188.
[46] A. Nezamzadeh-Ejhieh, N. Moazzeni, J. Ind. Eng. Chem., 19 (2013) 1433-1442.
[47] R.D. Kumar, R. Jayavel, J. Mater. Sci. - Mater. Electron., 25 (2014) 3953-3961.
[48] T. Rohani Bastami, A. Ahmadpour, F. Ahmadi Hekmatikar, J. Ind. Eng. Chem., 51 (2017) 244-254.
[49] P. Scherrer, Göttinger Nachrichten Math. Phys., (1918) 98-100.
[50] S. Tay, C. Huan, A. Wee, R. Liu, W. Goh, C. Ong, G. Chen, J. Vac. Sci. Technol. A, 20 (2002) 125-131.
[51] E. García-López, G. Marcì, F. Puleo, V. La Parola, L.F. Liotta, Appl. Catal., B., 178 (2015) 218-225.
[52] Y. Pei, W. Du, Y. Li, W. Shen, Y. Wang, S. Yang, S. Han, Phys. Chem. Chem. Phys. , 17 (2015) 18185-18192.
[53] S. Thirumalairajan, K. Girija, N.Y. Hebalkar, D. Mangalaraj, C. Viswanathan, N. Ponpandian, Rsc Adv., 3 (2013) 7549-7561.
[54] T. Caronna, F. Fontana, I.N. Sora, R. Pelosato, Mater. Chem. Phys., 116 (2009) 645-648.
[55] A. Schön, J.-P. Dacquin, C. Dujardin, P. Granger, Top. Catal., 60 (2017) 300-306.
[56] F. Parrino, E. García-López, G. Marcì, L. Palmisano, V. Felice, I.N. Sora, L. Armelao, J. Alloys Compd., 682 (2016) 686-694.
[57] H. Wang, L. Zhang, Z. Chen, J. Hu, S. Li, Z. Wang, J. Liu, X. Wang, Chem. Soc. Rev., 43 (2014) 5234-5244.
[58] S. Thirumalairajan, K. Girija, I. Ganesh, D. Mangalaraj, C. Viswanathan, A. Balamurugan, N. Ponpandian, Chem. Eng. J., 209 (2012) 420-428.
[59] S. Dong, K. Xu, G. Tian, J. Mater. Sci., 44 (2009) 2548-2552.
[60] S. Li, Y.-H. Lin, B.-P. Zhang, C.-W. Nan, Y. Wang, in Photocatalytic and magnetic behaviors observed in nanostructured BiFeO 3 particles, AIP, (2009).
[61] S. Thirumalairajan, K. Girija, V.R. Mastelaro, N. Ponpandian, New J. Chem., 38 (2014) 5480-5490.
[62] P. Xiao, J. Hong, T. Wang, X. Xu, Y. Yuan, J. Li, J. Zhu, Catal Lett, 143 (2013) 887-894.
[63] Q. Peng, B. Shan, Y. Wen, R. Chen, Int. J. Hydrogen Energy, 40 (2015) 15423-15431.
[64] C.S. Chen, T.C. Chen, C.C. Chen, Y.T. Lai, J.H. You, T.M. Chou, C.H. Chen, J.-F. Lee, Langmuir, 28 (2012) 9996-10006.
[65] S.M.N. Jeghan, J.Y. Do, M. Kang, J. Ind. Eng. Chem., (2017).
[66] W.Y. Jung, S.-S. Hong, J. Ind. Eng. Chem., 19 (2013) 157-160.
[67] L. Li, M. Zhang, P. Tian, W. Gu, X. Wang, Ceram. Int., 40 (2014) 13813-13817.
[68] J. Xu, Y. Li, B. Yuan, C. Shen, M. Fu, H. Cui, W. Sun, Chem. Eng. J., 291 (2016) 174-183.
[69] J. Herney-Ramirez, M.A. Vicente, L.M. Madeira, Appl. Catal., B., 98 (2010) 10-26.
[70] Y. Nie, L. Zhang, Y.-Y. Li, C. Hu, J. Hazard. Mater., 294 (2015) 195-200.
[71] Y. Zhang, J. Wan, Y. Ke, J. Hazard. Mater., 177 (2010) 750-754.
[72] S. Wang, Dyes Pigm., 76 (2008) 714-720.
[73] J. Zhang, X. Zhang, Y. Wang, RSC Adv., 6 (2016) 13168-13176.
[74] Y. Liu, H. Yu, S. Zhan, Y. Li, Z. Lv, X. Yang, Y. Yu, J. Sol-Gel Sci. Technol., 58 (2011) 716.
[75] H. Eskandarloo, A. Badiei, M.A. Behnajady, Ind. Eng. Chem. Res., 53 (2014) 6881-6895.
[76] J.-w. Shi, X. Yan, H.-J. Cui, X. Zong, M.-L. Fu, S. Chen, L. Wang, J. Mol. Catal. A: Chem., 356 (2012) 53-60.
[77] J. Zhang, Z. Ma, Mol. Catal. , 432 (2017) 285-291.
[78] Y. Wang, X. Cheng, X. Meng, H. Feng, S. Yang, C. Sun, J. Alloys Compd., 632 (2015) 445-449.

Figures:

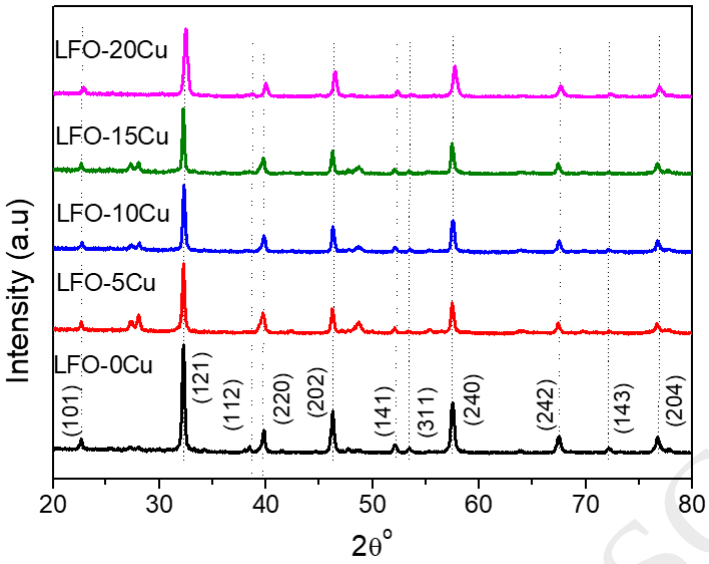

Fig. 1. XRD patterns of LFO and $LaFe_{1-x}Cu_xO_3$.

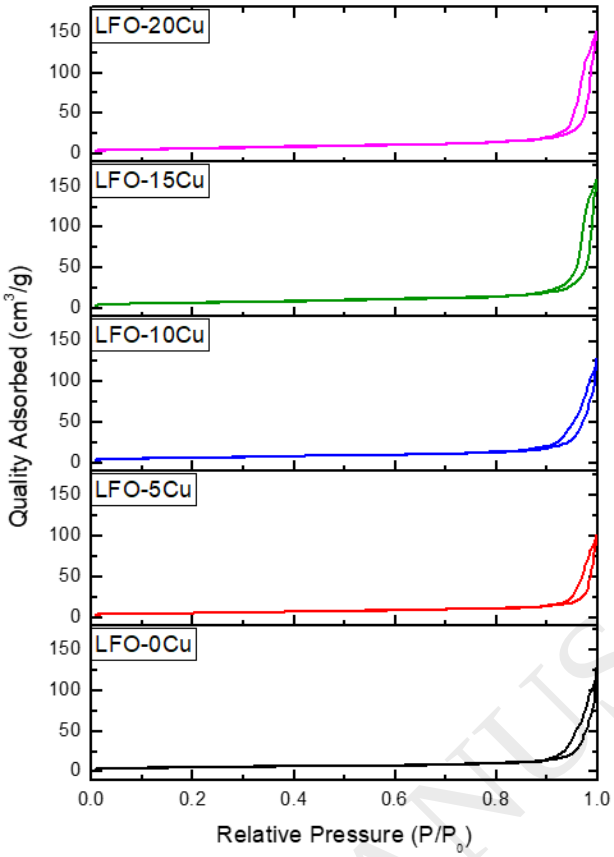

Fig. 2. N_2 adsorption-desorption isotherms of LFO and $LaFe_{1-x}Cu_xO_3$.

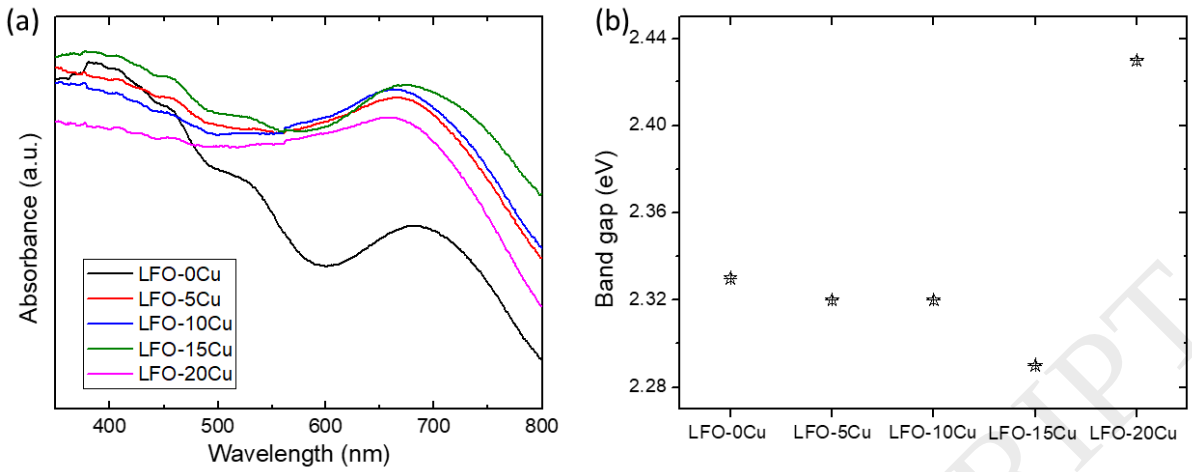

Fig. 3. (a) UV-vis absorption spectra and (b) corresponding bandgaps of LFO and $LaFe_{1-x}Cu_xO_3$.

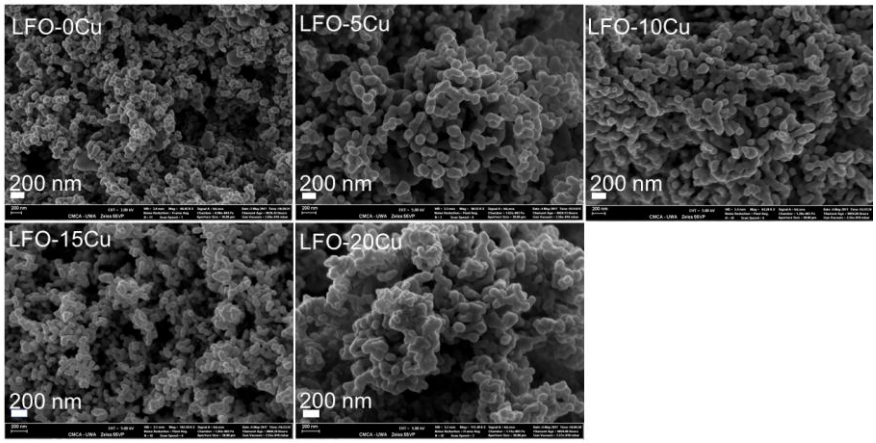

Fig. 4. SEM images of LFO and $LaFe_{1-x}Cu_xO_3$.

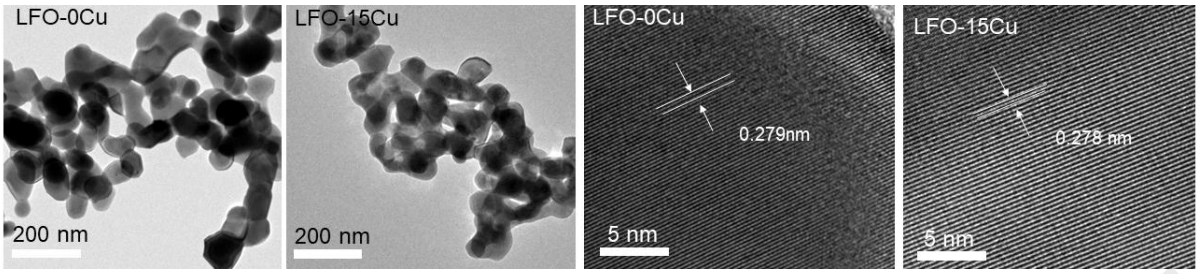

Fig. 5. TEM images of LFO-0Cu and LFO-15Cu.

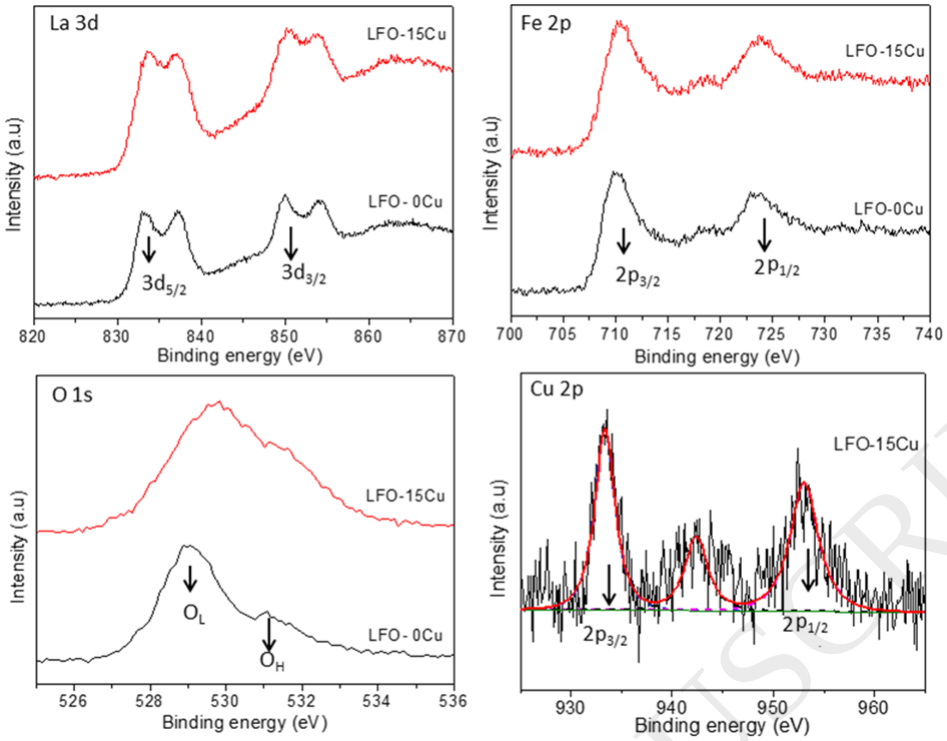

Fig. 6. XPS spectra of La 3d, Fe 2p, O 1s for LFO-0Cu and LFO-15Cu; and Cu 2p for LFO-15Cu.

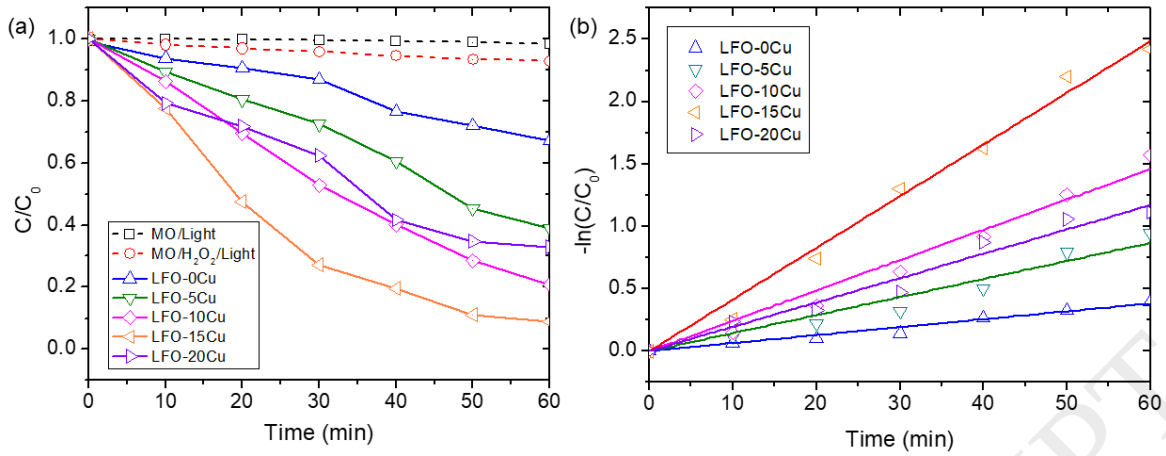

Fig. 7. (a) Photodegradation of MO as a function of illumination time by using LFO and $LaFe_{1-x}Cu_xO_3$ (reaction conditions: temperature = 25 °C; initial dye concentration = 10 mg/L; catalyst dosage = 1.0 g/L; initial H_2O_2 concentration = 0.3 g/L; initial pH = 6; NaCl = 0 M); and (b) plots of -ln (C/C_0) *versus* irradiation time.

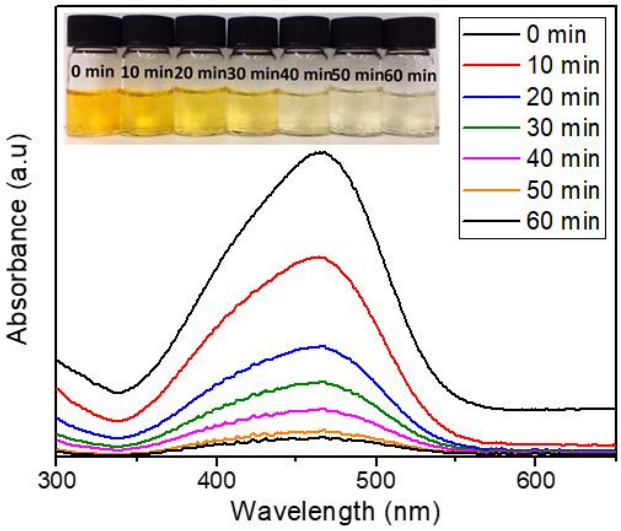

Fig. 8. Temporal UV-vis spectral change of MO aqueous solution *versus* irradiation time in the photo-Fenton reaction (the inset: colour change of MO solution *versus* irradiation time) (reaction conditions: temperature = 25 °C; initial dye concentration = 10 mg/L; catalyst dosage = 0.8 g/L; initial H_2O_2 concentration = 0.3 g/L; initial pH = 6; NaCl = 0 M).

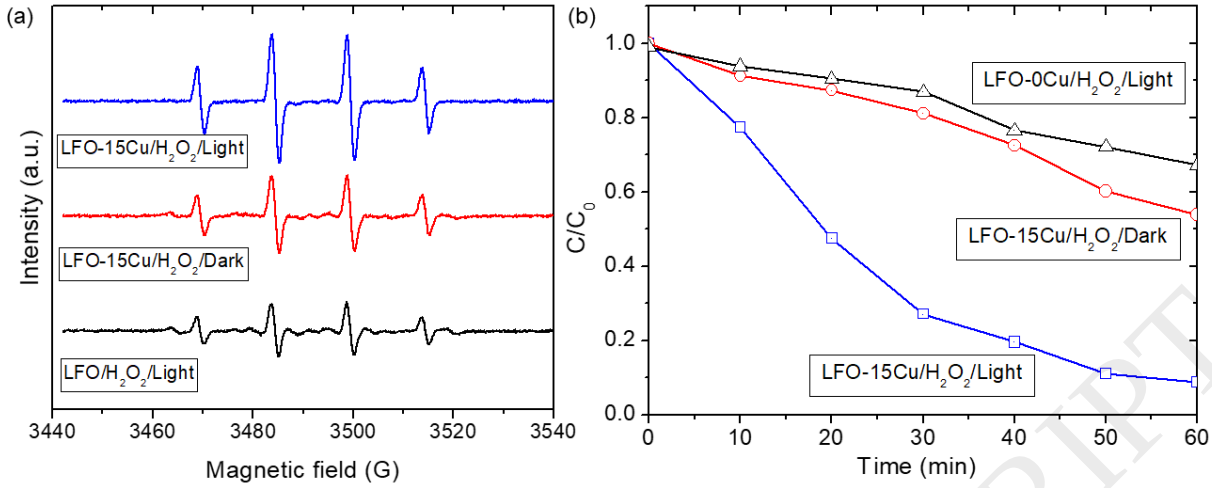

Fig. 9. (a) EPR spectra of DMPO-.OH adducts and (b) degradation of MO in the systems of LFO-15Cu/H_2O_2/Dark, LFO-15Cu/H_2O_2/Light and LFO/H_2O_2/Light.

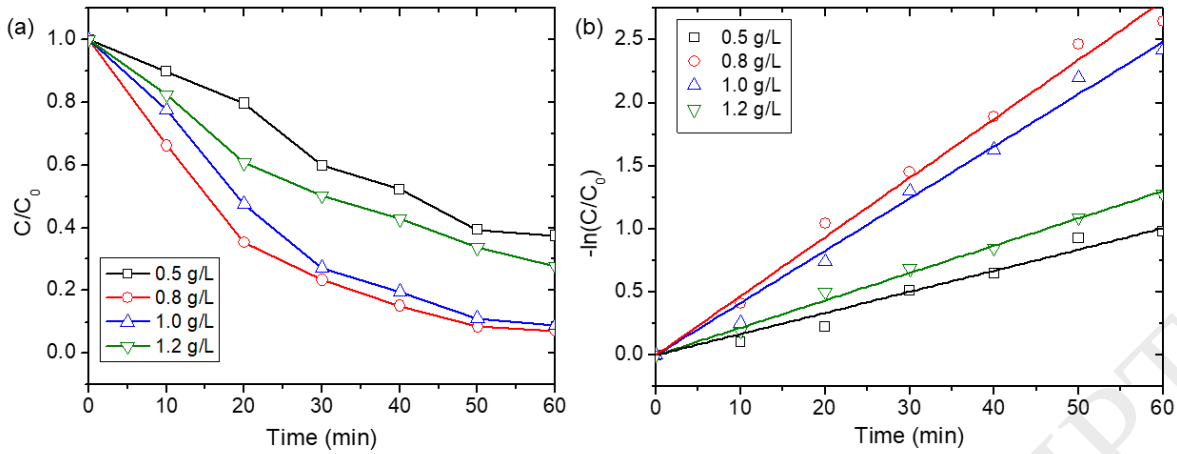

Fig. 10. (a) Effect of catalyst dosage on photodegradation of MO (reaction conditions: temperature = 25 °C; initial dye concentration = 10 mg/L; initial H_2O_2 concentration = 0.3 g/L; initial pH = 6; NaCl = 0 M) and (b) plots of -ln (C/C_0) *versus* irradiation time.

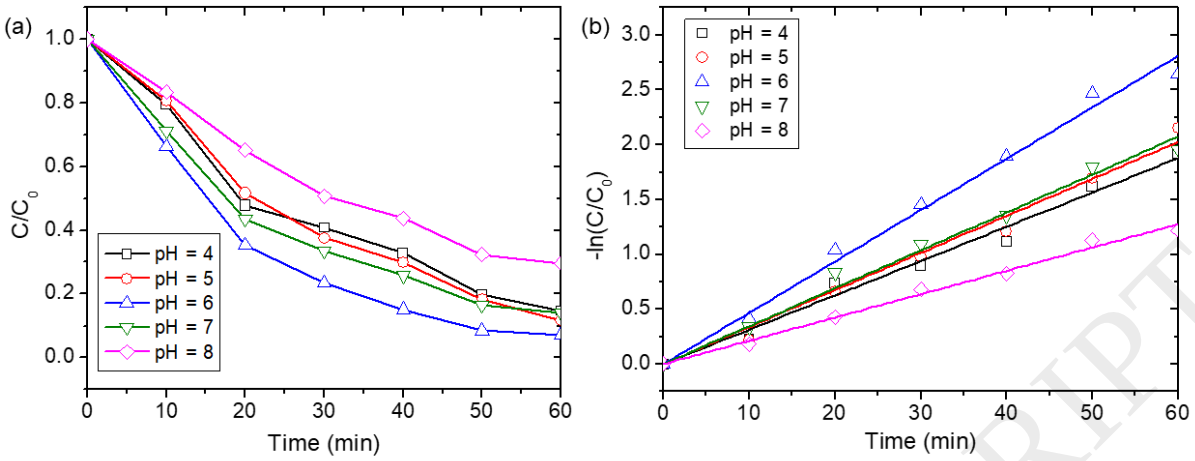

Fig. 11. (a) Effect of initial pH on photodegradation of MO (reaction conditions: temperature = 25 °C; initial dye concentration = 10 mg/L; catalyst dosage = 0.8 g/L; initial H_2O_2 concentration = 0.3 g/L; NaCl = 0 M) and (b) plots of -ln (C/C_0) *versus* irradiation time.

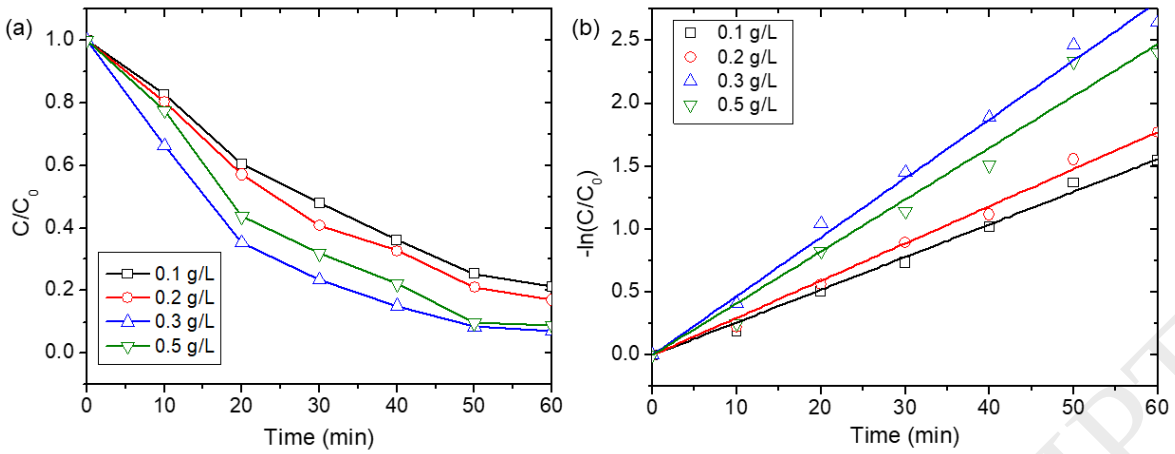

Fig. 12. (a) Effect of initial concentration of H_2O_2 on photodegradation of MO (reaction conditions: temperature = 25 °C; initial dye concentration = 10 mg/L; catalyst dosage = 0.8 g/L; initial pH = 6; NaCl = 0 M); and (b) plots of -ln (C/C_0) *versus* irradiation time.

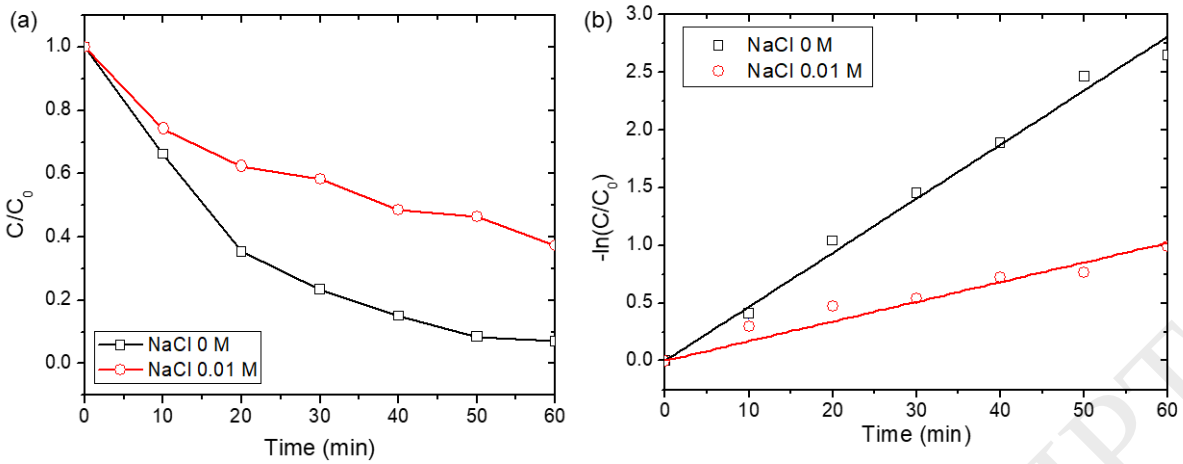

Fig. 13. (a) Effect of NaCl on photodegradation of MO (reaction conditions: temperature = 25 °C; initial dye concentration = 10 mg/L; catalyst dosage = 0.8 g/L; initial H_2O_2 concentration = 0.3 g/L; initial pH = 6) and (b) plots of -ln (C/C_0) *versus* irradiation time.

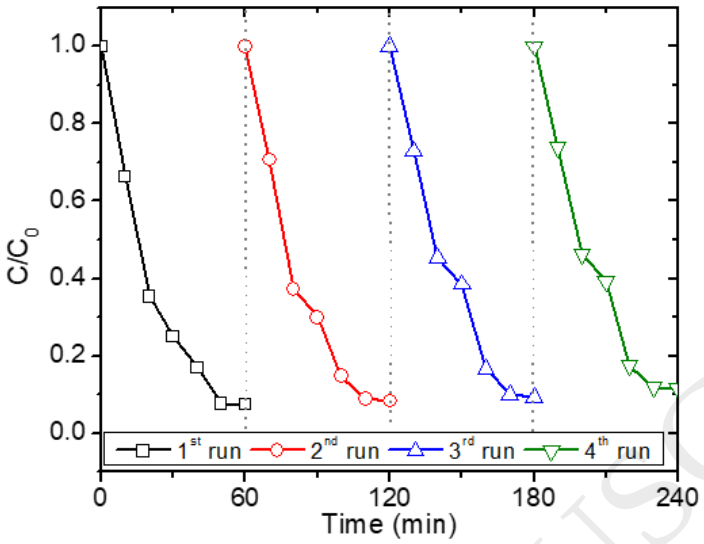

Fig. 14. Stability of LFO-15Cu over photo-Fenton catalytic degradation of MO in four cycling runs (reaction conditions: temperature = 25 °C; initial dye concentration = 10 mg/L; initial H_2O_2 concentration = 0.3 g/L; catalyst dosage = 0.8 g/L; initial pH = 6; NaCl = 0 M).

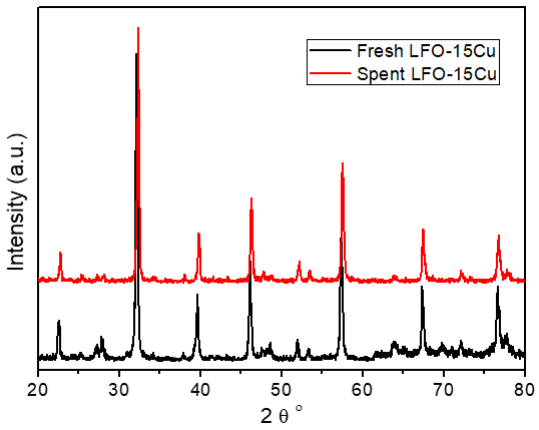

Fig. 15. XRD patterns of fresh LFO-15Cu before photo-Fenton catalytic degradation of MO and spent LFO-15Cu after 4 cycles of photo-Fenton catalytic degradation of MO.

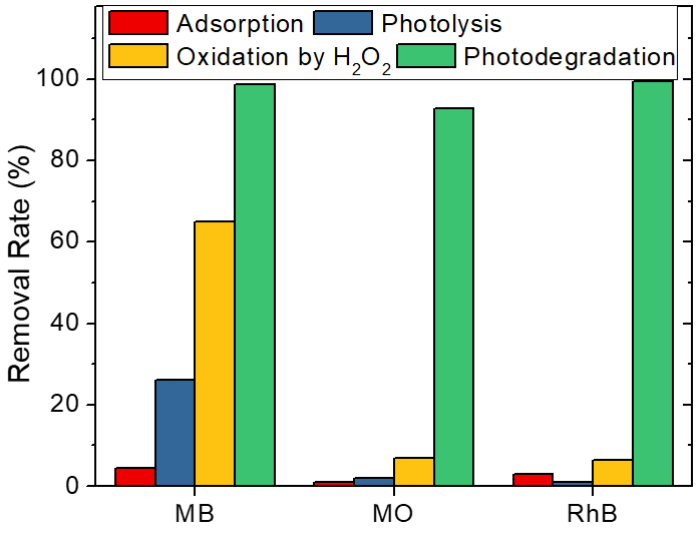

Fig. 16. Removal of MB, RhB and MO using LFO-15Cu *via* adsorption, photolysis, oxidation by H_2O_2 and photodegradation (reaction conditions: temperature = 25 °C, initial dyes concentration = 10 mg/L; catalyst dosage = 0.8 g/L, initial H_2O_2 concentration = 0.3 g/L; initial pH = 6; NaCl = 0 M).

Tables:

Table 1. Crystallite size, cell volume and lattice parameters of LFO and $LaFe_{1-x}Cu_xO_3$.

Sample	Lattice constant (Å)			Cell volume ($Å^3$)	Crystallite size (nm)
	a	*b*	*c*		
LFO-0Cu	5.5566	7.8446	5.5555	242.160	28.0
LFO-5Cu	5.5539	7.8409	5.5475	241.580	27.3
LFO-10Cu	5.5512	7.8372	5.5412	241.074	26.4
LFO-15Cu	5.5461	7.8185	5.5463	240.499	25.7
LFO-20Cu	5.5418	7.7850	5.5189	238.101	21.4

Table 2. Structural property and chemical composition of LFO and $LaFe_{1-x}Cu_xO_3$.

Sample	Structural property			Molar ratio	
	S_{BET} (m^2/g)	Pore volume (cm^3/g)	Pore size (nm)	Actual Cu/Fe	Theoretical Cu/Fe
LFO-0Cu	17.63	0.099	45.66	-	-
LFO-5Cu	19.01	0.068	32.90	0.05/0.95	0.05/0.95
LFO-10Cu	21.37	0.11	35.52	0.11/0.89	0.10/0.90
LFO-15Cu	25.33	0.12	39.29	0.14/0.86	0.15/0.85
LFO-20Cu	24.57	0.14	37.95	0.18/0.82	0.20/0.80

Table 3. Concentration of metal ions leaching from LFO-15Cu.

Ion species	Concentration (mg/L)
La	1.558
Fe	12.8×10^{-3}
Cu	0.482